

Demonstration of a Cut-Cell Representation of 3D Orography for Studies of Atmospheric Flows over Very Steep Hills

SARAH-JANE LOCK

Institute for Climate and Atmospheric Science, University of Leeds, Leeds, United Kingdom

HEINZ-WERNER BITZER

DWD, Offenbach am Main, Germany

ALISON COALS, ALAN GADIAN, AND STEPHEN MOBBS

National Centre for Atmospheric Science, University of Leeds, Leeds, United Kingdom

(Manuscript received 20 March 2011, in final form 3 August 2011)

ABSTRACT

Advances in computing are enabling atmospheric models to operate at increasingly fine resolution, giving rise to more variations in the underlying orography being captured by the model grid. Consequently, high-resolution models must overcome the problems associated with traditional terrain-following approaches of spurious winds and instabilities generated in the vicinity of steep and complex terrain.

Cut-cell representations of orography present atmospheric models with an alternative to terrain-following vertical coordinates. This work explores the capabilities of a cut-cell representation of orography for idealized orographically forced flows. The orographic surface is represented within the model by continuous piecewise bilinear surfaces that intersect the regular Cartesian grid creating cut cells. An approximate finite-volume method for use with advection-form governing equations is implemented to solve flows through the resulting irregularly shaped grid boxes.

Comparison with a benchmark orographic test case for nonhydrostatic flow shows very good results. Further tests demonstrate the cut-cell method for flow around 3D isolated hills and stably resolving flows over very steep orography.

1. Introduction

Since the early days of numerical weather prediction (NWP), terrain-following grids (e.g., Phillips 1957; Gal-Chen and Somerville 1975; Clark 1977) have been the preferred method for handling uneven orography in atmospheric models. The method deforms the vertical levels to fit around a smoothed representation of the surface topography—the extent of the deformation is greatest near the bottom of the model grid, relaxing to pure horizontal levels near the model top. Terrain-following approaches have been favored for so long because of their computational simplicity—operating on an effective

rectangular grid regardless of the shape of the underlying orography; the lowest vertical level always coinciding with the orographic surface, aiding surface flux computations; and the lowest few vertical levels being naturally positioned for application of a boundary layer scheme. As a result, such models have been used for mesh resolutions of $O(100)$ km in the early days of NWP to 1–20 km in today's models.

Many studies (e.g., Sundqvist 1976; Janjic 1989) have demonstrated problems with the terrain-following approach: generation of spurious winds in the vicinity of hills, and instabilities associated with distorted grid cells near steep orographic gradients. Until recently, the relatively coarse resolution of the grids (with respect to the detail of the underlying terrain) has prevented the errors associated with terrain-following approaches from causing major problems. However, with advances in computing technology enabling increasingly high-resolution studies

Corresponding author address: Sarah-Jane Lock, Institute for Climate and Atmospheric Science, School of Earth and Environment, University of Leeds, Leeds LS2 9JT, United Kingdom.
E-mail: s.j.lock@leeds.ac.uk

(both for research and operational forecasting), steeper and more sharply varying gradients are being resolved by the model grid, exposing the limitations of the terrain-following method.

The representation of hills with step-terrain vertical coordinates, where the size of the steps is defined by the grid spacing (e.g., Mesinger et al. 1988), has been explored. Gallus and Klemp (2000) demonstrate sharp disturbances in the flow above the step corners, which extend far up into the atmosphere for wide hills. Indeed, their analysis of the analytic solution confirms that such disturbances are an intrinsic part of the flow solution over steplike mountains. Using shallower steps to resolve the hill, both model and analytic solutions are seen to approach the smooth flows associated with a smooth hill. But for wide hills, the vertical resolution required to adequately describe smooth flow is far greater than that needed by a terrain-following coordinate. Furthermore, model solutions demonstrate erroneously weak flow in the lee of the hill, attributed to spurious vorticity generation at the step corners.

Proposals to represent uneven terrain with cut cells within the model grid (e.g., Adcroft et al. 1997; Bonaventura 2000; Steppeler et al. 2002) have demonstrated good accuracy for well-known 2D idealized flows. The method consists of embedding the terrain within the model grid, resulting in some grid cells that are cut by the orographic surface. In some instances, (e.g., Bonaventura 2000), the demonstrations have been limited to rectangular-shaped cut cells producing a steplike representation of the orography (described as “partial steps” in Adcroft et al. 1997). In contrast to the previously described step-terrain models, this approach enables a more accurate description of the hill for a given vertical grid spacing. A more generalized approach enables irregularly shaped cut cells resulting from piecewise linear representations of the terrain (e.g., Steppeler et al. 2002; Rosatti et al. 2005), which is the approach explored in this paper.

The potential for the cut-cell approach in a full NWP forecasting model is demonstrated in Steppeler et al. (2006)—comparison with an equivalent terrain-following model for real-data cases showed improved quantitative precipitation forecast scores; and for the cases examined, there was no evidence of reduced lee winds in the cut-cell model.

Recent work on cut-cell methods has focused on dealing with the so-called small-cell problem—the smallest cut-cell defining the restriction on the time step permissible for stability. Yamazaki and Satomura (2010) demonstrates a method for combining small cut-cells either horizontally or vertically with neighboring cells, and demonstrates good results for 2D flows over both shallow and steep slopes. An alternative approach is explored in

Klein et al. (2009) involving construction of a flux for the boundaries of the cut cells that can be applied stably over the time step defined by the regular grid.

In this paper, exploration of the cut-cell approach is extended to 3D idealized tests for very steep gradients. The cut-cell method is implemented in a “microscale model,” designed for very high-resolution studies [i.e., grid spacings of $O(100)$ m and less]. As discussed earlier in this section, very high-resolution grids capture more of the complexity of the underlying topography, making a cut-cell representation of orography a natural choice for a model for small-scale studies. The microscale model was intended as a research tool to complement larger-scale studies performed with the Met Office Unified Model (UM; Davies et al. 2005). Many of the model features were therefore informed by those of the UM. Particular features that differ from those of previously studied cut-cell models are the equation set and choice of prognostic variables, the choice of grid staggering, and the use of a fully explicit time-integration method (which is made appropriate by the similar grid resolutions in the horizontal and vertical for microscale studies).

Section 2 describes in detail the model—the governing equations and numerical discretizations, including a thorough description of the cut-cell approach. Results are presented in section 3 for a number of idealized orographic flow cases—initially, verified against a 2D benchmark case from the literature (Gallus and Klemp 2000), and subsequently extended to demonstrate its application to 3D cases and flows over very steep gradients. The results are discussed in section 4.

2. Model details

a. Governing equations and discretizations

The microscale model is a limited-area model intended for very high-resolution 3D studies—grid scales of ≤ 100 m in both the vertical *and* horizontal. The governing equations, based on Tapp and White (1976) and Cullen (1990), are appropriate for representing microscale dynamics—in particular, they are nonhydrostatic and in Cartesian form. They describe the evolution of the wind components u , v , and w ; potential temperature θ ; and pressure in terms of the Exner function:

$$\Pi = \left(\frac{p}{p_s} \right)^{R/c_p},$$

where p is pressure and the constants p_s , R , and c_p are surface pressure ($=10^5$ Pa), the dry gas constant and specific heat at constant pressure, respectively.

The dry atmosphere is assumed to obey the ideal gas law, in the following form:

$$\theta = \frac{1}{\rho} \frac{p_s}{R} \Pi^{(c_p/R-1)},$$

where ρ is density.

A steady background state, described by $\bar{\Pi}(z)$ and $\bar{\theta}(z)$, is defined, which is in hydrostatic balance:

$$\frac{d\bar{\Pi}}{dz} = -\frac{g}{c_p \bar{\theta}},$$

where g is the acceleration due to gravity. The equations for the pressure and temperature fields can then be posed in terms of perturbations, Π' and θ' , from the background state, such that

$$\Pi = \bar{\Pi}(z) + \Pi'(\mathbf{x}, t),$$

$$\theta = \bar{\theta}(z) + \theta'(\mathbf{x}, t).$$

The model equations become

$$\frac{\partial u}{\partial t} + c_p \bar{\theta} \frac{\partial \Pi'}{\partial x} = -\mathbf{u} \cdot \nabla u + f v - F w - c_p \theta' \frac{\partial \Pi'}{\partial x}, \quad (1)$$

$$\frac{\partial v}{\partial t} + c_p \bar{\theta} \frac{\partial \Pi'}{\partial y} = -\mathbf{u} \cdot \nabla v - f u - c_p \theta' \frac{\partial \Pi'}{\partial y}, \quad (2)$$

$$\frac{\partial w}{\partial t} + c_p \bar{\theta} \frac{\partial \Pi'}{\partial z} - \frac{\theta}{\bar{\theta}} = -\mathbf{u} \cdot \nabla w + F u - c_p \theta' \frac{\partial \Pi'}{\partial z}, \quad (3)$$

$$\frac{\partial \Pi'}{\partial t} + (\gamma - 1) \bar{\Pi} \nabla \cdot \mathbf{u} - \frac{g w}{c_p \bar{\theta}} = -\mathbf{u} \cdot \nabla \Pi' - (\gamma - 1) \Pi' \nabla \cdot \mathbf{u}, \quad (4)$$

$$\frac{\partial \theta'}{\partial t} + w \frac{\partial \bar{\theta}}{\partial z} = -\mathbf{u} \cdot \nabla \theta', \quad (5)$$

where $\gamma = c_p/c_v$, for the specific heat at constant volume c_v .

As discussed in Thuburn et al. (2002), the “ f - F plane” approximation of the Coriolis force, which includes both horizontal and vertical components, is adopted for additional accuracy with negligible loss of efficiency.

A fully compressible description of the atmosphere is chosen to avoid the need to solve a 3D elliptic equation, which becomes especially difficult on the irregular grid that results from the cut-cell representation of orography.

The discretized equations are solved using an Eulerian, fully explicit approach; a fully explicit approach being justifiable since grid resolutions for the microscale model are of the same order of magnitude in both the horizontal and vertical. A time-splitting method (based on Klemp and Wilhelmson 1978) is applied to deal with the fastest waves—acoustic and buoyancy terms, on the left-hand side of the above equations, are integrated using a short time step with a second-order forward–backward scheme; while

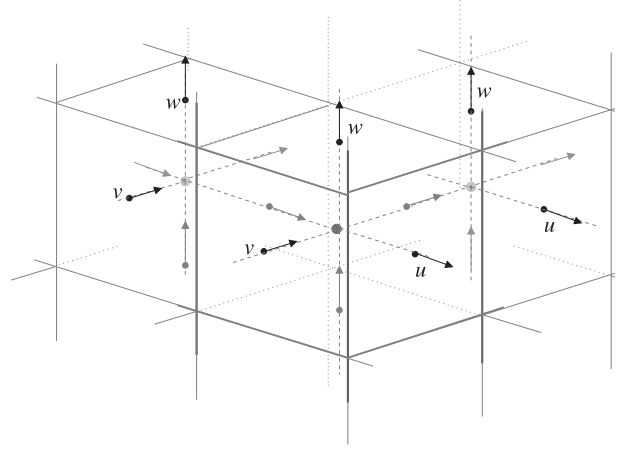


FIG. 1. Illustration of the storage locations for the model variables on a staggered grid: at the center of each grid box is stored Π' , denoted by a filled circle; u , v , and w are stored on the gridbox faces perpendicular to their flow directions.

the other terms (on the right-hand side) are integrated on a longer time step using the leapfrog scheme, stabilized with a Robert–Asselin filter (Robert 1966; Asselin 1972). The spatial discretization takes the form of second-order-centered differencing, with fourth-derivative explicit numerical diffusion applied to the advected variables to stabilize the second-order schemes. A staggered grid is chosen for storage of the model variables (see Fig. 1)— Π' is stored at the center of each grid box, while u , v , and w are stored on the gridbox faces, half a grid-length distant in the x , y , and z directions, respectively; θ' is collocated with w .

b. Lower boundary

Following Steppeler et al. (2006), a 3D uneven lower boundary is represented with piecewise bilinear surfaces, that connect continuously at grid-column boundaries. For the grid column centered on (i, j) , the orographic heights at the four corners of the grid column—that is, at $(i \pm 1/2, j \pm 1/2)$ —define a unique bilinear surface, illustrated in Fig. 2 and described by

$$h(x, y) = m_1 x + m_2 xy + m_3 y + c, \quad (6)$$

where m_1 , m_2 , m_3 , and c are constants that can be determined from knowing the heights at the four corners.

The result is some grid boxes near the model bottom that are wholly beneath the lower boundary; and some that are *cut* by the lower boundary [e.g., the grid box centered on (i, j, k) in the figure], leaving only a fraction of the gridcell volume open to the atmosphere. For grid cells that are totally beneath the orographic surface, no model solutions are computed. To solve flows through the irregularly shaped cut cells, an approximate finite-volume approach is taken following Steppeler et al. (2002). The method invokes Gauss's theorem:

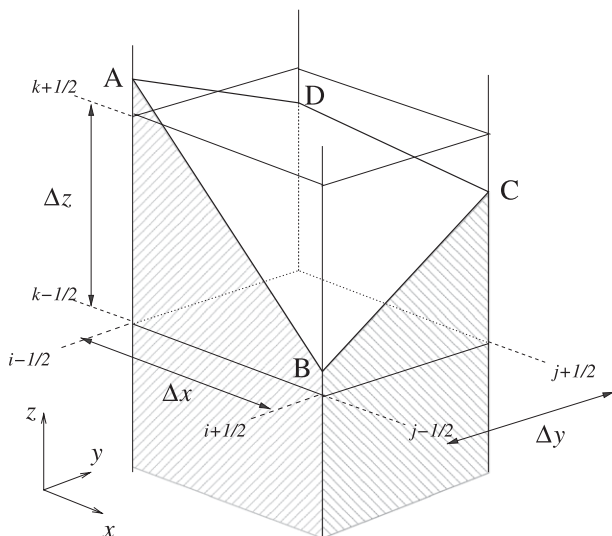


FIG. 2. The orographic heights at the four corners of the grid column centered on (i, j) —marked ABCD—define a unique bilinear surface, which results in the grid box (i, j, k) being cut by the orography.

$$\int_V (\nabla \cdot \mathbf{u}) dV = \oint_{\partial V} \mathbf{u} \cdot d\mathbf{a}, \quad (7)$$

where $d\mathbf{a}$ is the unit vector normal to the element of area on surface ∂V acting away from volume V , to equate the flow divergence in a single grid box [arising in Eq. (4)] to the fluxes across the gridbox faces.

Under a finite-volume method, a model solution stored at a specified grid location represents a mean value for the entire grid volume or face (e.g., the u solution stored at

the center of a grid face represents the mean flow through the entire grid face). Consider the cut cell centered on (i, j, k) in Fig. 2: at the center of the face cut by orographic surface BC is stored velocity component $u(i + 1/2, j, k)$, which is therefore taken to represent the flow across the fraction of the grid face that is open to the atmosphere.

Since the velocity components act perpendicularly to the gridbox surface on which they are stored, they are readily positioned for computing the fluxes out of the grid box. Equation (7) is therefore simple to solve for all grid boxes—cut or uncut. For an uncut grid cell, the sum of fluxes out of the grid cell can be computed directly from the u , v , and w components stored on the gridcell faces. For a cut cell, the u , v , and w components stored on the cut faces continue to represent the fluxes across the open fraction of those surfaces. In addition, the flux across the bilinear surface that represents the orography is required. Since the lower boundary does not act as a source of mass to the atmosphere, the flux across the surface must always be zero.

The discrete divergence in the cell centered on (i, j, k) therefore becomes

$$D_{i,j,k} \equiv (\nabla \cdot \mathbf{u})_{i,j,k} = \frac{1}{dV'_{i,j,k}} \{ (udA'_u)_{i+1/2,j,k} + (vdA'_v)_{i,j+1/2,k} + (wdA'_w)_{i,j,k+1/2} - (udA'_u)_{i-1/2,j,k} - (vdA'_v)_{i,j-1/2,k} - (wdA'_w)_{i,j,k-1/2} \}, \quad (8)$$

where dV' is the volume of the cell that is open to the atmosphere; dA'_u is the area of the cell face on which u is stored that is open to the atmosphere; and dA'_v and

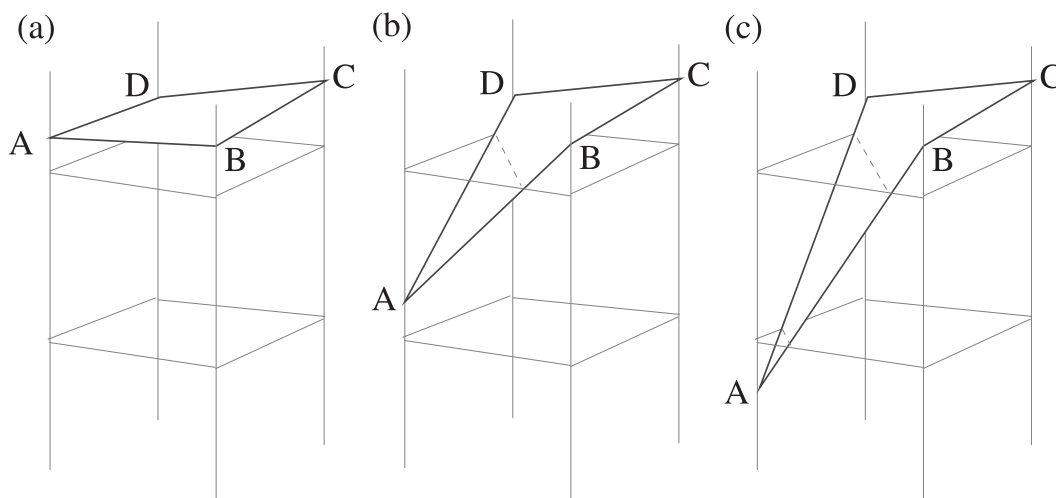


FIG. 3. Relative to any given grid cell, the height of the lower boundary at each of the four grid-column corners (ABCD) have three possible positions: above, within, or below the grid cell, resulting in $3^4 = 81$ topologically distinct configurations for the lower boundary. The figure illustrates three examples for (a) A above, (b) A within, and (c) A below the grid cell; while BCD all remain above.

dA'_w are similarly defined for the faces on which v and w , respectively, are stored.

It is clear that for an uncut grid cell, where

$$dV' = \Delta x \Delta y \Delta z, \quad dA'_u = \Delta y \Delta z, \quad dA'_v = \Delta x \Delta z, \\ dA'_w = \Delta x \Delta y,$$

Eq. (8) reduces to a centered finite-difference expression for $\nabla \cdot \mathbf{u}$.

The advection terms are modified to take account of the cut cells by introducing factors that scale the flux across a cell face by the ratio of the open face to a regular uncut face (e.g., for advective velocity u), the associated flux limiter is defined as

$$F_u = dA'_u / \Delta y \Delta z.$$

The x -direction advection of quantity ϕ at cell center i, j, k becomes

$$u \frac{\partial \phi}{\partial x} = \overline{F_u u \delta_x \phi}^x, \quad (9)$$

where

$$\delta_x \phi_i \equiv (\phi_{i+1/2,j,k} - \phi_{i-1/2,j,k}) / \Delta x, \\ \overline{\phi}_i^x \equiv (\phi_{i-1/2,j,k} + \phi_{i+1/2,j,k}) / 2;$$

and similarly for the y and z directions.

For an uncut cell, the flux limiters take value 1 and the advection calculation Eq. (9) reduces to a centered finite-difference expression for a regular grid.

The discrete form of the equations is set out in full in appendix A.

In practice, specifying the location and shape of the lower boundary and computing the resulting cut-cell volumes and surface areas is not trivial. The lower boundary surface is determined by specifying the heights of the surface at the four vertices of the grid column and using Eq. (6) to define the respective bilinear surface. Relative to a given grid cell within that column, the surface heights at the four corners can each take three positions: above, within or below the grid cell—some examples are shown in Fig. 3. In total, for any grid cell, there are $3^4 = 81$ potential configurations for the resulting surface in relation to the grid cell—that is, three relative positions (above, within, and below) for each of the four corner heights. Two of those 81 potential positions will not result in the grid cell of interest being cut: all four corner heights *above* the top of the grid cell (see Fig. 3a), and all four corner heights *below* the bottom of the grid cell. That leaves

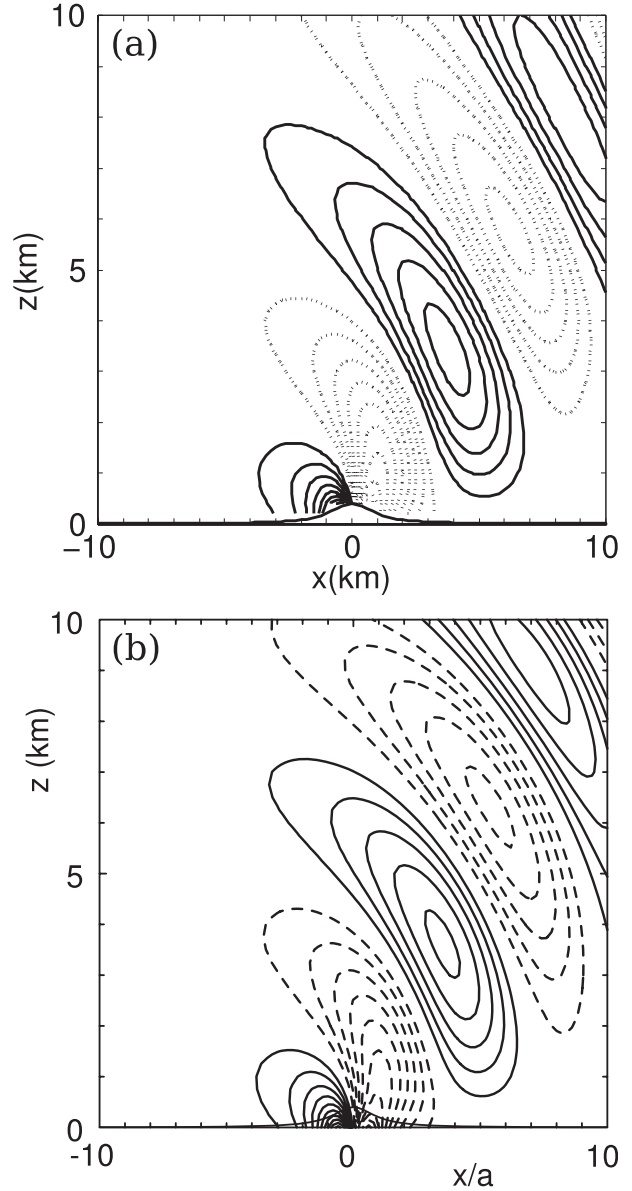


FIG. 4. Vertical velocity field for flow over a bell-shaped hill of height 400 m and half-width 1000 m, with contour interval of 0.25 m s^{-1} and positive values indicated by solid lines, negative values by dashed lines: (a) the cut-cell model results after 40 000 integrations and (b) the analytic solution for a smooth hill reproduced from (Gallus and Klemp 2000, see their Fig. 1c).

79 possible orientations of cut cell—a formidable challenge to formulate within the model code.

The approach to specifying the shape and location of the lower boundary in this model is to compute the cut-cell volumes and surface areas by dividing a grid cell (of dimensions $\Delta x \times \Delta y \times \Delta z$) into lots of very narrow columns (each of dimension $\delta x \times \delta y \times \Delta z$, where $\Delta x = M\delta x$ for integer M ; similarly for y). Within each narrow

column, the height of the true surface at the horizontal center ($\delta x/2, \delta y/2$) is applied as a constant height across the whole column. In so doing, the bilinear surface across a whole *grid* column is approximated by lots of small, horizontal steps built from rectangular prisms (like the Giant's Causeway, which is the coastal region in northern Ireland characterized by basalt stone columns: <http://www.nationaltrust.org.uk/main/w-giantscauseway>). The approach leads to an approximation in the cut-cell volume calculations, though the error tends to zero as M (the number of divisions defining the narrow columns) increases. The advantage with the method is that it enables a single code implementation to compute the volumes and surface areas for all possible cut-cell configurations. Full details of the approach are set out in appendix B.

c. Small-cell problem

As is widely recognized in the literature, cut-cell methods suffer from the so-called small-cell problem (Klein et al. 2009), whereby the permitted time step for the time integrations is defined by the smallest cut cell, which could be arbitrarily small, forcing a prohibitively small time step. Several papers propose methods for avoiding the problem—(e.g., Yamazaki and Satomura 2010; Klein et al. 2009; Steppeler et al. 2002; Adcroft et al. 1997). This study does not attempt to address the small-cell problem. For each of the model experiments, the time integrations are performed using a time step determined from the size of the smallest cut cell, making the necessary time steps very small. Much computational efficiency could be gained by adopting one of the methods cited above, but this paper concentrates on demonstrating the performance of cut cells for idealized cases in 3D and with a very steep slope.

3. Results

a. A benchmark 2D orographic test case

A benchmark 2D test case is used to demonstrate the accuracy of the model. The test case is for flow in a stably stratified atmosphere past a bell-shaped hill that generates nonhydrostatic waves, earlier studied in Gallus and Klemp (2000).

The shape of the hill is described by

$$h(x) = \frac{h_0}{(1 + x^2/a^2)}, \quad (10)$$

where h_0 is the maximum hill height of 400 m, and the hill half-width $a = 1000$ m. The stratified background state is defined by a constant Brunt–Väisälä frequency

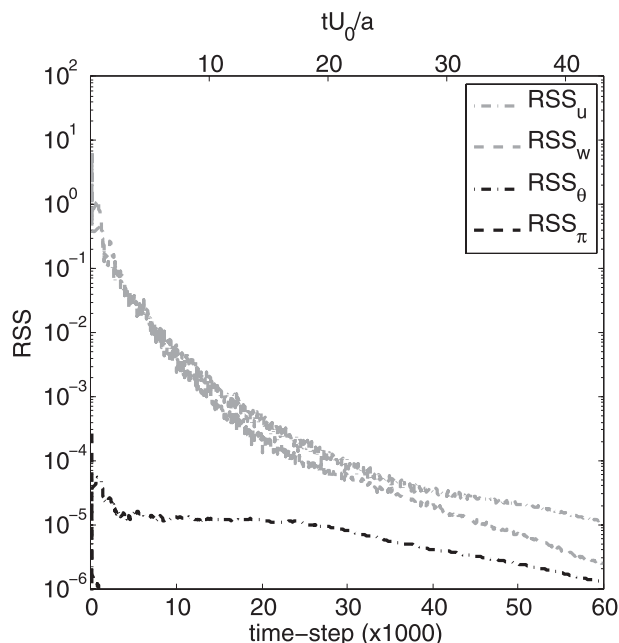


FIG. 5. RSS values for each model field plotted for every time step (up to IT = 60 000) for the 2D bell-shaped hill benchmark test case. The values provide a measure of the drift in solutions over the entire model domain between consecutive time steps—see Eq. (13). The upper axis indicates a nondimensionalized time, specified in terms of U_0 and a .

of $N = 0.01 \text{ s}^{-1}$ and a sea level potential temperature of $\bar{\theta}_0 = 293.15 \text{ K}$; and the initial flow condition is $(U_0, W_0) = (10, 0) \text{ m s}^{-1}$ everywhere.

For the model setup, the horizontal grid spacing is fixed at $\Delta x = 0.2a = 200 \text{ m}$ (following Gallus and Klemp). The vertical grid spacing is $\Delta z = 200 \text{ m}$. The model domain is a total of 60 km ($300\Delta x$) wide and 16 km ($80\Delta z$) deep. To avoid disturbance from waves reflected at the model boundaries, absorbing layers are included—in the outermost 6 km (30 grid spacings) for the upper boundary and 10 km (50 grid spacings) for the lateral boundaries. Within the absorbing layers, a damping term is applied to model solution ϕ (representing u, v, w, θ') at new time n in the following form:

$$\phi^{\text{damped}} = \phi^n + (\alpha_x + \alpha_z)(\phi^n - \phi^0), \quad (11)$$

where ϕ^0 is the initial state of ϕ , and α_x and α_z are the damping coefficients. The strength of α_x varies through the absorbing layer as

$$\alpha_x = \begin{cases} -\frac{\alpha_x^{\text{max}}}{2} \left[1 - \cos\left(\pi \frac{x - x_0}{x_n - x_0}\right) \right], & \text{if } x_0 \leq x \leq x_n; \\ 0, & \text{otherwise,} \end{cases} \quad (12)$$

where x_0 and x_n are the positions of the inner and outer edges, respectively, of the absorbing layer at the lateral boundary; α_t^{\max} represents the upper limit on the strength of the damping layer; and α_z for the absorbing layer at the upper model boundary varies similarly with respect to z .

To perform this 2D experiment with the 3D cut-cell model, the model is setup with three grid points and periodic boundary conditions in the y direction, with $\Delta y = 200$ m; the initial model fields include no variation in the y direction—in particular, there is zero initial wind component acting in the y direction, no Coriolis force is applied, and the 2D hill described by Eq. (10) becomes a 2D ridge. Results presented in this paper are from the central x – z slice. Though not presented here, model results show no variation in the y direction, and $v = 0$ m s^{−1} is maintained throughout the model integrations.

Gallus and Klemp (2000) derive the analytic solution for the smooth hill described by Eq. (10). Figure 4 includes a reproduction of the analytic solution from Gallus and Klemp for comparison with equivalent results from the cut-cell model at time step IT = 40 000.

The model results compare well with the analytic solution. The position and amplitude of the wave are in good agreement. In particular, there is no evidence from the cut-cell model of noise generated at the lower boundary by discontinuities in the orographic surface gradients, despite a relatively coarse vertical resolution—there being only two grid levels to the top of the hill. This contrasts significantly to results from step representations of orography. For a similarly dimensioned hill, Gallus and Klemp (2000) demonstrate both the analytic solution and model results with the hill represented by two steps each of height Δz ($\Delta z = 200$ m)—see Figs. 1b and 7a, respectively, in their paper. One can see from their presentation of the analytic solution, that significant disturbance to the flow is generated directly above the sharp corners of the step hill. The model results show similarly noisy features unless very shallow steps are used (i.e., a very fine vertical resolution is applied through the depth of the hill).

To provide insight into the convergence (or otherwise) of the model solutions toward some steady state, a measure based on a residual sum of squares (RSS) has been studied for each model field. The measure considers the drift from one time step to the next over the whole model domain. For the model field ϕ , the RSS value at time step n is given by the sum over all grid points (i, j, k):

$$\text{RSS}_\phi = \sum_{i,j,k} (\phi_{i,j,k}^n - \phi_{i,j,k}^{n-1})^2. \quad (13)$$

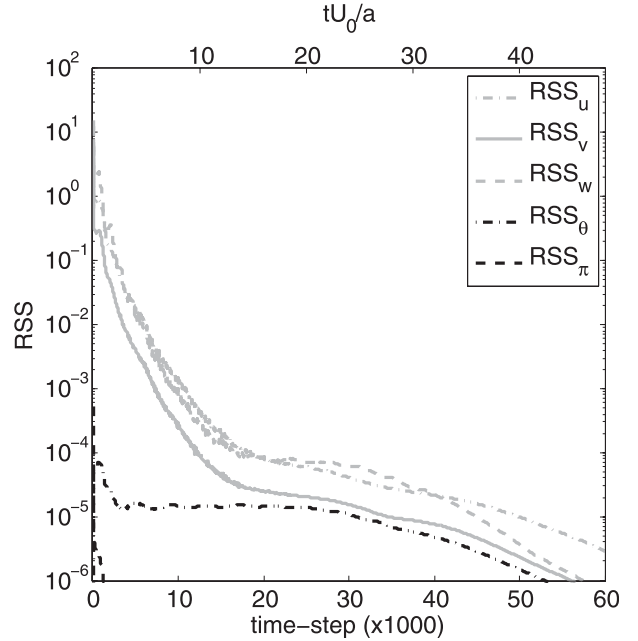


FIG. 6. RSS values for each model field plotted for every time step (up to IT = 60 000) for the case of the 3D medium-steep bell-shaped hill (half-width $a = 1$ km).

The RSS values provide a quantitative measure, offering some objectivity in choosing an appropriate model time for presentation and comparison of model results. Figure 5 shows plots of the RSS values for all model fields at each time step. The plots show a clear decrease in the RSS values for all model fields throughout the model run time. (Note the logarithmic scale on the vertical axis.) A rapid decrease during the first 15 000 time steps is followed by a slower decrease thereafter. By IT = 40 000, the noise apparent in the wind field values has reduced and values for all fields are very small: $<10^{-4}$. Consequently, model outputs at time step 40 000 are chosen for comparison with the analytic solution in Fig. 4. Though not shown here, there is little change in the model solutions when considered at later model times. For context, the upper axis of the plot shows the nondimensional time, specified in terms of the background wind and hill half-width: tU_0/a (as used in Dudhia 1993). As noted earlier, for these studies, the length of time step is limited by the smallest cut cell, making the time steps very small. The plot time of 40 000 time steps is equivalent to $28.8a/U_0$ (comparable to that used to reach a steady solution in Dudhia 1993).

b. Flow past a 3D medium-steep bell-shaped hill

To demonstrate the 3D implementation of the cut-cell representation of orography, an extension of the earlier

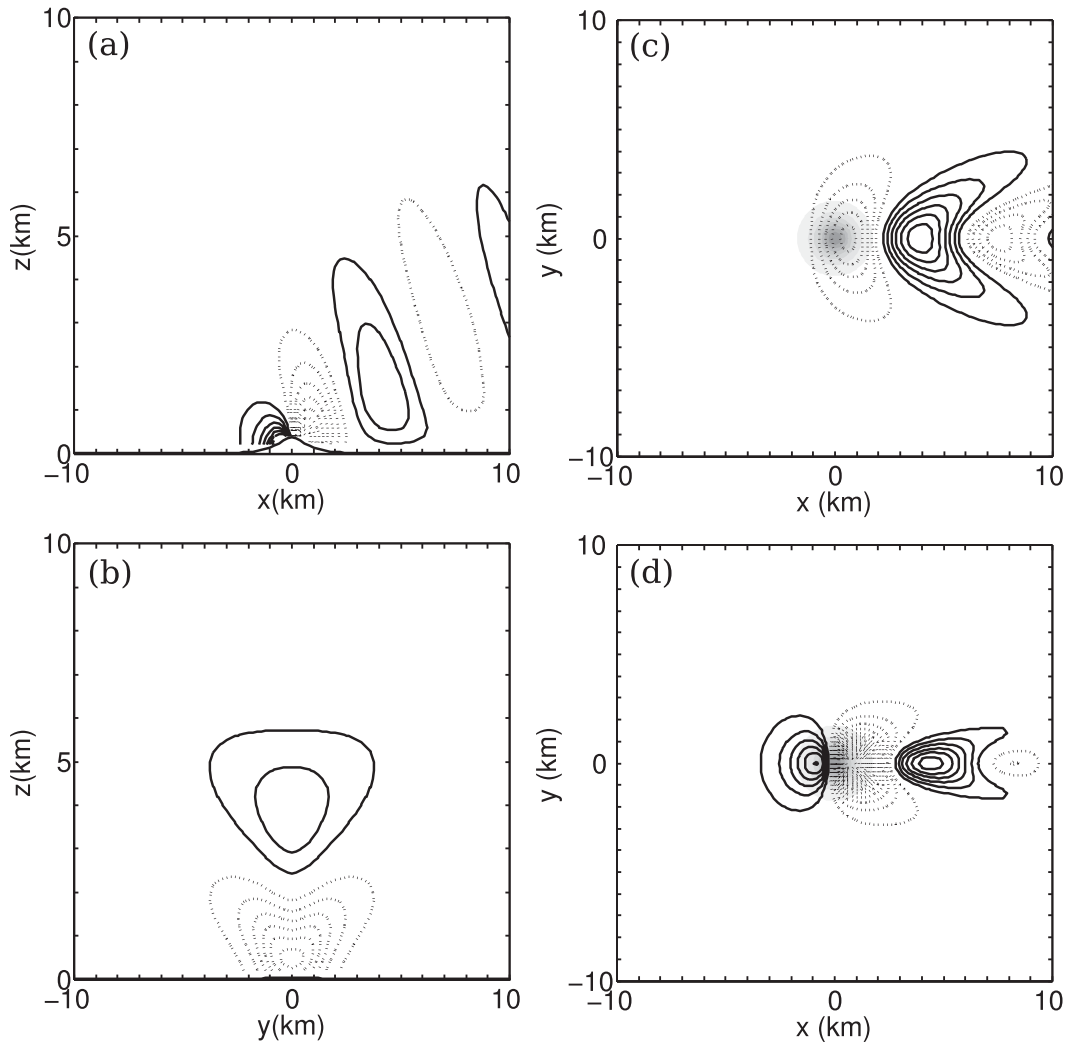


FIG. 7. Model results for the vertical velocity field for flow over the 3D medium-steep bell-shaped hill of height 400 m and half-width 1000 m; positive values are indicated by solid lines, negative values by dashed lines: (a) a vertical x - z slice through the center of the hill; (b) a vertical y - z slice 2 km downstream of the top of the hill; (c) and (d) horizontal x - y slices at heights $z = 2000$ m and $z = 800$ m, respectively, with the shaded contours indicating the position of the underlying hill. (a)–(d) Model solutions are represented at IT = 20 000 integrations. Contour intervals: (a) 0.25 and (b)–(d) 0.10 m s^{-1} .

2D bell-shaped hill is presented here. It comprises flow around an isolated bell-shaped hill, described by

$$h(x, y) = \frac{h_0}{(1 + x^2/a^2 + y^2/a^2)^{3/2}}, \quad (14)$$

where the maximum height of the hill $h_0 = 400$ m and the half-width $a = 1000$ m. The general shape of the hill is chosen to agree with that analyzed in Smith (1980), with dimensions equivalent to those of the earlier 2D case.

The initial state of the atmosphere for this case is identical to that described for the 2D case with the flow initialized to be $(U_0, V_0, W_0) = (10, 0, 0) \text{ m s}^{-1}$

everywhere. For this idealized case, the Coriolis force is not included.

The grid spacings, domain lengths and absorbing layers for this case are as described for the 2D case for the horizontal x and vertical z directions. In the y direction, the domain length is 40 km with grid spacing $\Delta y = 200$ m, and an absorbing layer in the outer 10 km (50 grid lengths), which takes the same form as described by Eq. (12).

The evolution of the RSS values for all model fields for this case can be seen in Fig. 6. As for the earlier case, there is a period of sharp decrease and some noise in the values during the first 15 000 steps. By IT = 20 000, values for all fields are very small ($< 10^{-4}$). Based on

the RSS plot, model fields for this case are presented at $IT = 20\,000$, though results at later times show little variation.

Figure 7 includes plots of the flow fields for the 3D case. The results successfully demonstrate stable and smooth solutions over many integrations. Horizontal slices above the hill for heights 2000 and 800 m (Figs. 7c and 7d, respectively) and a vertical cross section 2000 m downstream of the hill (Fig. 7b) show a flow field that is symmetric about the hill. A vertical cross section parallel to the background flow, through the center of the hill (Fig. 7a) shows a wave propagating upward from the top of the hill. Unlike for the 2D case, the wave is seen to decay rapidly with height. The general shape of the field agrees with that analyzed from linear theory in Smith (1980). Smith focuses on analysis of the hydrostatic regime—that is, $Na/U \gg 1$ —and demonstrates that the vertical displacement field aloft includes a “U shaped” region of downward motion on the lee side of the hill. For the nonhydrostatic regime, where $Na/U = 1$ —the flow regime for this case—Smith includes a diagram showing that the field undergoes damped oscillations farther downstream. Such motion is clearly evident from the plots in Fig. 7. In particular, the horizontal slice in Fig. 7d is chosen to be at a very similar height to that discussed by Smith. The apparent wavelength of the downstream motion is comparable to that described by Smith: approximately 7 km compared to $2\pi U_0/N \approx 6.3$ km.

c. Flow past a very steep isolated hill

The final demonstration is for flow over a very narrow, steep hill. The hill takes the form of the previously studied 3D bell-shaped hill, but in this case, the height $h_0 = 400$ m and the half-width $a = 100$ m (i.e., an aspect ratio of $h_0/a = 4.0$ and a maximum gradient of 74° from the horizontal). The horizontal grid spacing for this case is scaled with the hill (as for the earlier cases) giving $\Delta x = \Delta y = 0.2a = 20$ m. In the vertical, a grid spacing of $\Delta z = 200$ m continues to be used.

The domain length and absorbing layers in terms of grid spacings, and the initial conditions are as described for the earlier 3D case. As before, the model was run out to 60 000 time steps. Figure 8 shows the evolution of the RSS values. The plot indicates that by $IT = 15\,000$, values for all fields are $< 10^{-4}$.

The vertical velocity fields after 15 000 model integrations are displayed in Fig. 9. The plots show several cross sections through the domain: a vertical slice through the center of the hill, parallel to the background wind in Fig. 9a; vertical slices perpendicular to the wind direction at 100 m up- and downstream of the hill top in Figs. 9b and 9c, respectively; and in Figs. 9d and 9e,

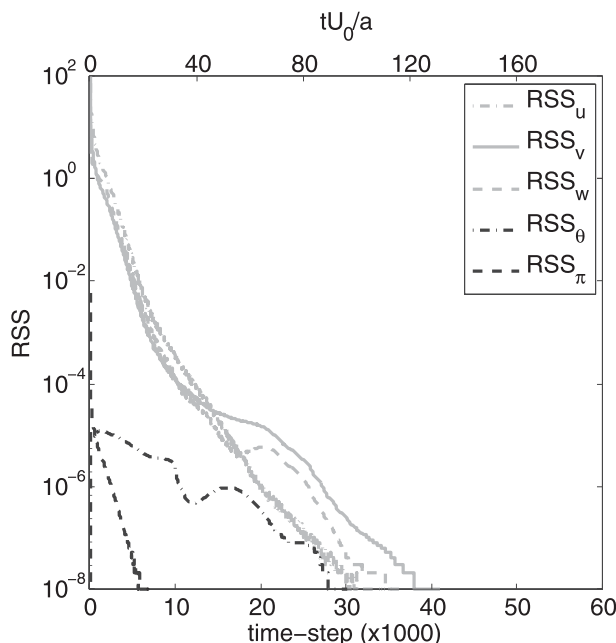


FIG. 8. RSS values for each model field plotted for every time step (up to $IT = 60\,000$) for the very steep isolated hill case.

horizontal slices at heights of 400 (i.e., at the hill top) and 200 m, respectively.

According to theory, for a case such as this where $Na/U \ll 1$, buoyancy forces become less important and the motion approaches potential flow (e.g., demonstrated in Satomura et al. 2003; Dudhia 1993). The vertical slice from the model results in Fig. 9a does indeed show motion like potential flow, with little disturbance of the background flow aloft. For this 3D case, Figs. 9b–e confirm that the results are symmetric about the $y = 0$ axis.

Looking in detail at the flow field near the hill some grid-scale noise on the upstream side of the hill is apparent, though no such problem is visible on the downstream side. The vertical slice perpendicular to the flow direction on the upstream side (Fig. 9b) illustrates the noise as a small disturbance in the otherwise smooth flow, noticeable at a height of 400–500 m. Similarly, the horizontal cross sections show the disturbance is visible at height 400 m, but there is little sign of any noise at 200 m (Figs. 9d,e). On the downstream side, all figures show a smooth field.

4. Conclusions

The cut-cell approach, using piecewise bilinear surfaces to represent uneven 3D orography, has been demonstrated as a method for simulating microscale atmospheric flows.

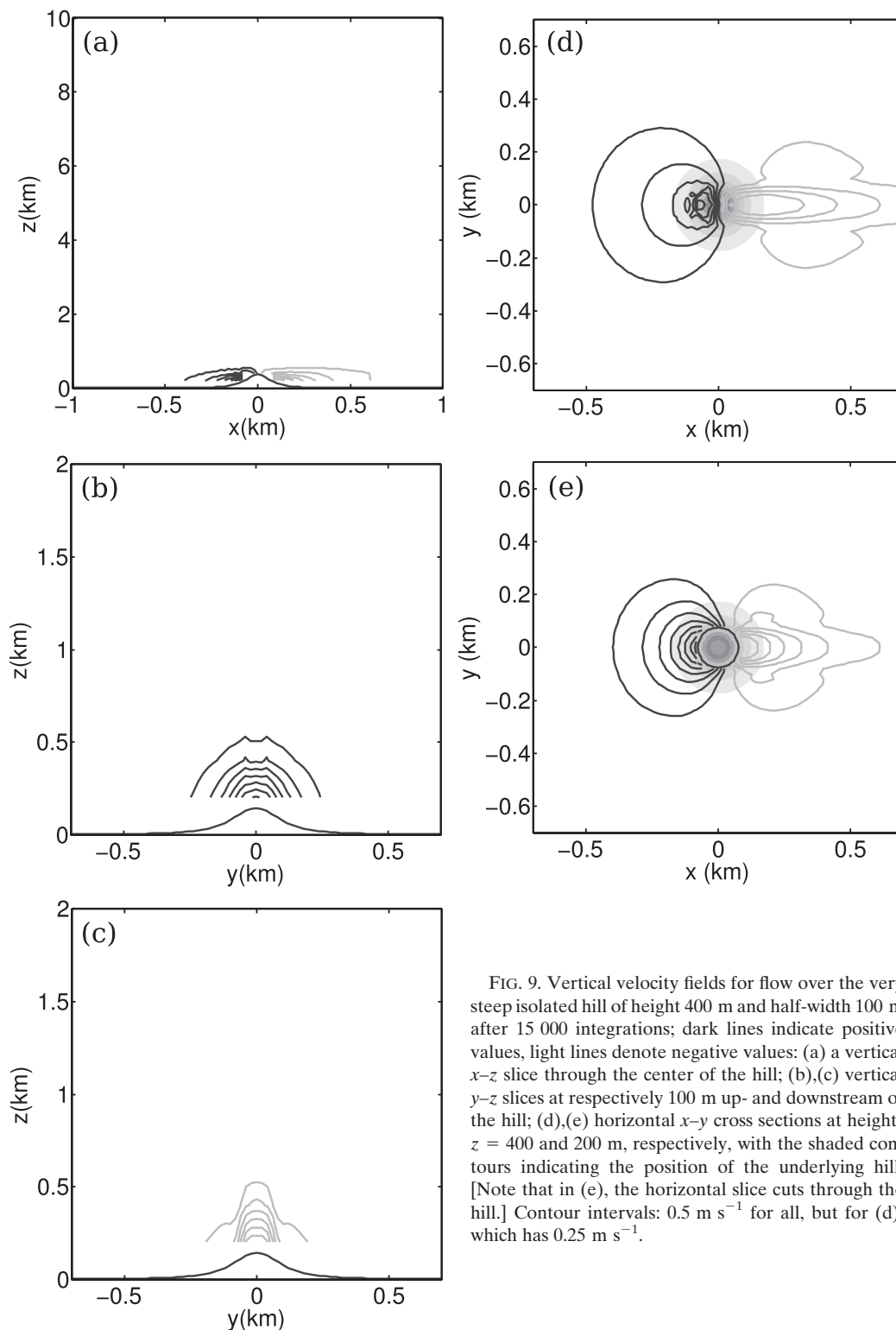


FIG. 9. Vertical velocity fields for flow over the very steep isolated hill of height 400 m and half-width 100 m after 15 000 integrations; dark lines indicate positive values, light lines denote negative values: (a) a vertical x - z slice through the center of the hill; (b),(c) vertical y - z slices at respectively 100 m up- and downstream of the hill; (d),(e) horizontal x - y cross sections at heights $z = 400$ and 200 m, respectively, with the shaded contours indicating the position of the underlying hill. [Note that in (e), the horizontal slice cuts through the hill.] Contour intervals: 0.5 m s^{-1} for all, but for (d), which has 0.25 m s^{-1} .

Results from the cut-cell model are shown to compare well with an analytic solution from Gallus and Klemp (2000) for a benchmark 2D case for nonhydrostatic flow. In contrast to the step representation of

orography considered by Gallus and Klemp (2000), the cut-cell model produces smooth results near the lower boundary, even for a relatively coarse vertical grid resolution.

The cut-cell method has been successfully implemented in 3D. Results for flow around an isolated hill of similar dimensions to the 2D case show stable, smooth flow fields including well-resolved features that are predicted by theory.

For a much steeper isolated hill (aspect ratio of 4.0), the cut-cell method continues to generate stable results over many integrations. As predicted by theory, the case produces potential flow. There is evidence of some grid-scale noise in the model solutions on the upstream side of the hill, which is confined to a small region at around the hill height. The downstream field is smooth.

Further work is needed to understand the limits for generating smooth and stable results from the cut-cell method; and for flows around a wider range of obstacles. Work is ongoing to contribute further investigations into the impact of methods that permit longer time steps—in particular, focusing on the “thin-wall approximation” (Steppeler et al. 2002). In addition, work is under way to explore the potential of the cut-cell model for moist dynamics, through extension of the governing equations to predict water vapor and liquid water mixing ratios.

Acknowledgments. Thanks to Jürgen Steppeler and Andrew Ross for helpful discussions. The authors also acknowledge support from the U.K. Natural Environment Research Council (NERC) for the Microscale Modelling project and the use of HECToR supercomputer time.

APPENDIX A

Discretized Equations for Use with Cut Cells

The discrete form of governing equations (1)–(5) is presented. The grid staggering is outlined in section 2: Π at the gridcell centers; u , v , and w on cell faces perpendicular to their flow direction; and θ collocated with w . Using the notation for averaging and differencing that is defined in section 2b, the equations become

$$\begin{aligned} \frac{\partial u}{\partial t} + c_p \bar{\theta}^z \delta_x \Pi' &= -\overline{F_u^x \bar{u}^x \delta_x u} - \overline{F_v^x \bar{v}^x \delta_y u} \\ &\quad - \overline{F_w^x \bar{w}^x \delta_z u} + f \bar{v}^x - F \bar{w}^x \\ &\quad - c_p \bar{\theta}'^z \delta_x \Pi', \end{aligned} \quad (\text{A1})$$

$$\begin{aligned} \frac{\partial v}{\partial t} + c_p \bar{\theta}^z \delta_y \Pi' &= -\overline{F_u^y \bar{u}^y \delta_x v} - \overline{F_v^y \bar{v}^y \delta_y v} \\ &\quad - \overline{F_w^y \bar{w}^y \delta_z v} - f \bar{u}^y - c_p \bar{\theta}'^z \delta_y \Pi', \end{aligned} \quad (\text{A2})$$

$$\begin{aligned} \frac{\partial w}{\partial t} + c_p \bar{\theta} \delta_z \Pi' - g \frac{\theta'}{\theta} &= -\overline{F_u^z \bar{u}^z \delta_x w} - \overline{F_v^z \bar{v}^z \delta_y w} \\ &\quad - \overline{F_w^z \bar{w}^z \delta_z w} + F \bar{u}^z \\ &\quad - c_p \theta' \delta_z \Pi', \end{aligned} \quad (\text{A3})$$

$$\begin{aligned} \frac{\partial \Pi'}{\partial t} + (\gamma - 1) \bar{\Pi} D - \frac{g \bar{w}^z}{c_p \bar{\theta}^z} &= -\overline{F_u \delta_x \Pi'} \\ &\quad - \overline{F_v \delta_y \Pi'} - \overline{F_w \delta_z \Pi'} \\ &\quad - (\gamma - 1) \Pi' D, \end{aligned} \quad (\text{A4})$$

$$\begin{aligned} \frac{\partial \theta'}{\partial t} + \overline{F_w^z \bar{w}^z \delta_z \theta'} &= -\overline{F_u^z \bar{u}^z \delta_x \theta'} - \overline{F_v^z \bar{v}^z \delta_y \theta'} \\ &\quad - \overline{F_w^z \bar{w}^z \delta_z \theta'}, \end{aligned} \quad (\text{A5})$$

where the discrete form of the divergence, $D \equiv (\nabla \cdot \mathbf{u})$, and flux limiters, F_u, F_v, F_w , are defined in section 2b.

At grid points near the lower boundary, where averages would include grid points on grid faces that are entirely subterrain, only the above-terrain points are used. In particular, considering the advection terms, this approach results in using a one-sided difference close to the boundary. For example, consider the calculation of the horizontal advection for wind component u_i , illustrated in Fig. A1. In Fig. A1a, the grid face at $i + 1$ is partially open to the atmosphere, and therefore, u_{i+1} stores information about the flow through the open part of the face, and is used in the following computation:

$$\left(u \frac{\partial u}{\partial x} \right)_i = \left(\overline{F_u^x \bar{u}^x \delta_x u} \right)_i.$$

In Fig. A1b, the entire grid face at $i + 1$ is submerged. Therefore, there is no flow information at u_{i+1} . In this case, the advection computation for u_i becomes a one-sided difference using only information from u_i and u_{i-1} :

$$\left(u \frac{\partial u}{\partial x} \right)_i = \left(\overline{F_u^x \bar{u}^x \delta_x u} \right)_{i-1/2}.$$

To calculate the pressure gradient terms for the u , v , and w integrations, no special consideration is made in the cut cells. To be precise, considering again Fig. A1a, on the cut grid face at $i + 1$, the model solution stored at u_{i+1} represents the mean flow through the open part of the grid face. Similarly, the pressure points at the center of the two grid cells separated by the grid face at $i + 1$ (i.e., cell centers $i + 1/2$ and $3/2$) store pressure solutions taken to represent the pressure in the open part of the cells. It is therefore clear that on any grid face that is open to the atmosphere (even if only partially), there must be a solution stored on that face for the associated wind vector, and

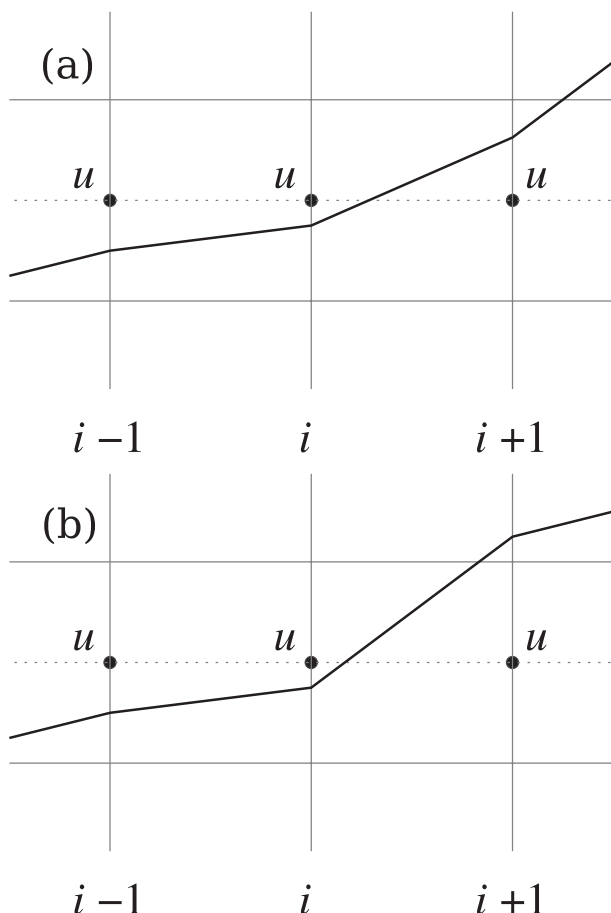


FIG. A1. To compute the horizontal advection at $u(i)$: (a) information from both $u(i \pm 1)$ is used and (b) only $u(i - 1)$ is used since the grid face at $i + 1$ is entirely beneath the surface.

there must be pressure solutions stored in the grid cells on either side of the grid face. It is these solutions that are used for the pressure gradient computation, applied over an entire grid length, regardless of the shape of the cut cells; hence, for the case illustrated in Fig. A1a, the pressure gradient at u_{i+1} would be calculated as

$$\frac{\Pi'_{i+3/2} - \Pi'_{i+1/2}}{\Delta x}.$$

APPENDIX B

Computing the Geometric Characteristics of the Cut Cells for a 3D Orographic Surface

To facilitate a simple generic method for computing a cell volume and surface areas for all potential cut-cell topologies (for bilinear surfaces), an approximate method is used that involves summing over small volume elements. Consider the grid cell centered on (i, j, k) of dimensions $\Delta x \times \Delta y \times \Delta z$. Each lateral grid face (those located at

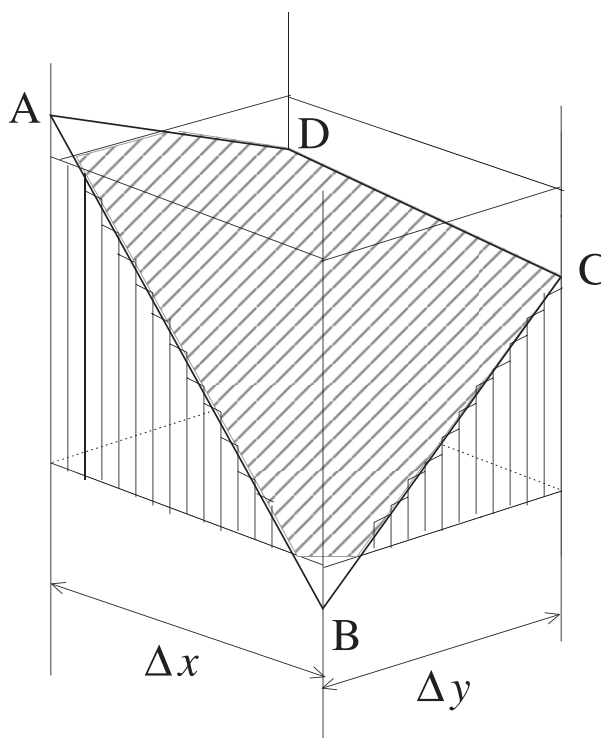


FIG. B1. To ease computation of the cut-cell volumes, each grid cell is divided into $M \times M$ narrow grid columns or volume elements. Within each volume element the true bilinear orographic surface is approximated with a constant height.

$i \pm \frac{1}{2}$ and $j \pm \frac{1}{2}$) are divided into M equal lengths, defining a total of M^2 tall, thin volume elements, each of dimension $\Delta x/M \times \Delta y/M \times \Delta z$ —indicated in Fig. B1.

The height of the orographic surface that is associated with each volume element is taken to be constant. It is fixed at the height of the bilinear surface at the horizontal center of the volume element. Figure B2a illustrates an example for volume element “A” with the horizontal center $(x_c, y_c)_A$. The height of the bilinear orographic surface at the volume-element center, $h(x_c, y_c)_A$, is known from Eq. (6). The true bilinear surface within a grid column is therefore approximated by M^2 discontinuous horizontal surfaces.

For the grid cell centered on (i, j, k) , the submerged part of the grid cell can be established by comparing the orographic height h at each volume element with the heights of the top and bottom of the grid cell, $z(k \pm \frac{1}{2})$. Figure B2b illustrates the submerged parts for three different volume elements. Labeled as A is an example where the orographic height is above the top of the grid cell [i.e., $h_A > z(k \pm \frac{1}{2})$]. Therefore, within grid cell (i, j, k) , the height of the submerged part for volume-element A is equal to the height of the grid box itself: $H_A = \Delta z$. Element “B” is an example of the orographic height

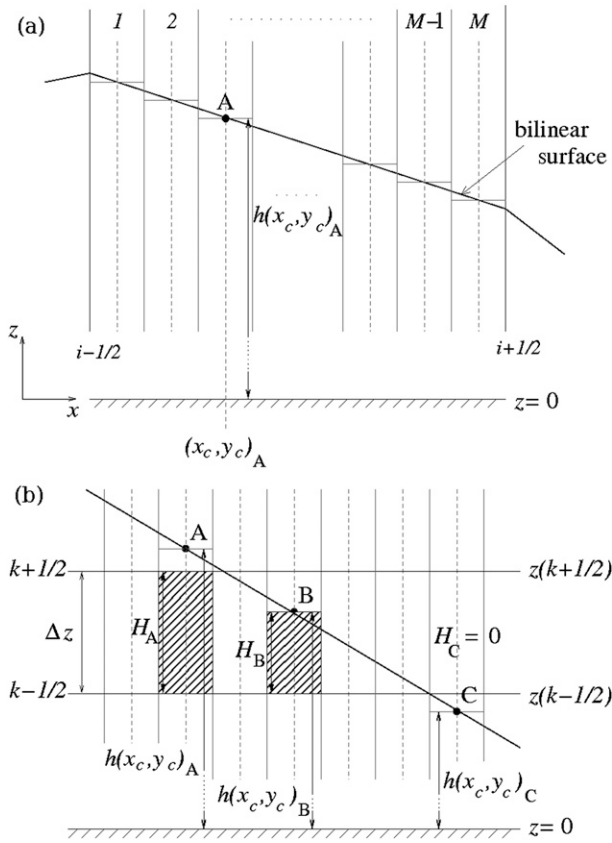


FIG. B2. A vertical x - z slice through the grid column centered on (i, j) shows the grid column divided in the x direction into M equally spaced narrow columns. (Division also occurs in the y direction, not shown.) (a) Within each narrow column, the bilinear surface is approximated by a constant height that is equal to the true height h at the horizontal center, (x_c, y_c) , of the column—illustrated for column “A.” Over the entire grid column, the true surface is represented by many small horizontal steps. (b) For the cut cell centered on (i, j, k) , the submerged part of the grid cell is identified by comparing $h(x_c, y_c)$ for each column with the heights at the top and bottom of the grid cell, $z(k \pm 1/2)$. The height H of the submerged part of each volume element that lies within grid cell (i, j, k) is computed. For element A, the orographic height is above the top of the grid cell, therefore, $H_A = \Delta z$. Columns B and C show cases where the orographic surface lies within and below the grid cell, respectively, such that $0 < H_B < \Delta z$ and $H_C = 0$.

being partway between the top and bottom of the grid cell. The height of the submerged part of the volume element within the grid cell (i, j, k) can be computed from the height of the bottom of the grid cell subtracted from the height of the orographic surface: $H_B = h_B - z(k - 1/2)$. Finally, “C” indicates a case where the orographic surface falls below the bottom of the grid cell [i.e., $h_C < z(k - 1/2)$], and therefore, the height of the submerged part within the grid cell (i, j, k) is $H_C = 0$.

Computing the volume of the submerged part of a volume element is straightforward: volume of a cuboid with

width, depth, and height of $\Delta x/M$, $\Delta y/M$, H , respectively. Consequently, the cut-cell volume—that is, the volume of the part of the grid cell that is open to the atmosphere—is the sum over all the volume elements’ submerged volumes subtracted from the full gridcell volume:

$$dV'_{i,j,k} = \Delta x \Delta y \Delta z - \sum_{I,J=1}^M \frac{\Delta x \Delta y}{M} H_{I,J}. \quad (\text{B1})$$

Cut-cell surface areas are computed in a similar manner. By using the volume elements already defined for the volume calculation, the submerged part of the lateral faces (at $i \pm 1/2$ and $j \pm 1/2$) can be established—in this instance representing the line where the bilinear surface intersects the gridcell face with a series of small horizontal steps. (Consider Fig. B2b to be representing the gridcell face at, e.g., $j - 1/2$.) For the upper and lower faces, a count is made of the number of volume elements for which the height of the orographic surface h is above the height of the gridcell face [e.g., for the face at $k + 1/2$, where $h_c > z(k + 1/2)$]. Summing over the volume elements that are fully submerged at face $k + 1/2$, each with area $\Delta x/M \times \Delta y/M$, reveals the area of the remainder of the gridcell face that is open to the atmosphere.

REFERENCES

- Adcroft, A., C. Hill, and J. Marshall, 1997: Representation of topography by shaved cells in a height coordinate ocean model. *Mon. Wea. Rev.*, **125**, 2293–2315.
- Asselin, R., 1972: Frequency filter for time integrations. *Mon. Wea. Rev.*, **100**, 487–490.
- Bonaventura, L., 2000: A semi-implicit semi-Lagrangian scheme using the height coordinate for a nonhydrostatic and fully elastic model of atmospheric flows. *J. Comput. Phys.*, **158**, 186–213.
- Clark, T., 1977: A small-scale dynamic model using a terrain-following coordinate transformation. *J. Comput. Phys.*, **24**, 186–215.
- Cullen, M. J. P., 1990: A test of a semi-implicit integration technique for a fully compressible non-hydrostatic model. *Quart. J. Roy. Meteor. Soc.*, **116**, 1253–1258.
- Davies, T., M. J. P. Cullen, A. J. Malcolm, M. H. Mawson, A. Staniforth, A. A. White, and N. Wood, 2005: A new dynamical core for the Met Office’s global and regional modelling of the atmosphere. *Quart. J. Roy. Meteor. Soc.*, **131**, 1759–1782.
- Dudhia, J., 1993: A nonhydrostatic version of the Penn State–NCAR mesoscale model: Validation tests and simulation of an Atlantic cyclone and cold front. *Mon. Wea. Rev.*, **121**, 1493–1513.
- Gal-Chen, T., and R. C. J. Somerville, 1975: On the use of a coordinate transformation for the solution of the Navier-Stokes equations. *J. Comput. Phys.*, **17**, 209–228.
- Gallus, W. A., and J. Klemp, 2000: Behavior of flow over step orography. *Mon. Wea. Rev.*, **128**, 1153–1164.
- Janjic, Z. I., 1989: On the pressure gradient force error in σ -coordinate spectral models. *Mon. Wea. Rev.*, **117**, 2285–2292.
- Klein, R., K. R. Bates, and N. Nikiforakis, 2009: Well-balanced compressible cut-cell simulation of atmospheric flow. *Philos. Trans. Roy. Soc. London*, **367A**, 4559–4575.

- Klemp, J. B., and R. B. Wilhelmson, 1978: The simulation of three-dimensional convective storm dynamics. *J. Atmos. Sci.*, **35**, 1070–1096.
- Mesinger, F., Z. I. Janjic, S. Nickovic, D. Gavrilov, and D. Deaven, 1988: The step-mountain coordinate: Model description and performance for cases of alpine lee cyclogenesis and for a case of an Appalachian redevelopment. *Mon. Wea. Rev.*, **116**, 1493–1518.
- Phillips, N. A., 1957: A coordinate system having some special advantages for numerical forecasting. *J. Meteor.*, **14**, 184–185.
- Robert, A., 1966: The integration of a low order spectral form of the primitive meteorological equations. *J. Meteor. Soc. Japan*, **44**, 237–244.
- Rosatti, G., D. Cesari, and L. Bonaventura, 2005: Semi-implicit, semi-Lagrangian modelling for environmental problems on staggered Cartesian grids with cut cells. *J. Comput. Phys.*, **204**, 353–377.
- Satomura, T., T. Iwasaki, K. Saito, C. Muroi, and K. Tsuboki, 2003: Accuracy of terrain following coordinates over isolated mountain: Steep Mountain Model Intercomparison Project (St-MIP). *Annu. Disaster Res. Inst. Kyoto Univ.*, **46B**, 337–346. [Available online at <http://www.dpri.kyoto-u.ac.jp/dat/nenpo/no46/46b0/a46b0t33.pdf>.]
- Smith, R. B., 1980: Linear theory of stratified hydrostatic flow past an isolated mountain. *Tellus*, **32**, 348–364.
- Steppeler, J., H. Bitzer, M. Minotte, and L. Bonaventura, 2002: Nonhydrostatic atmospheric modeling using a z -coordinate representation. *Mon. Wea. Rev.*, **130**, 2143–2149.
- , and Coauthors, 2006: Prediction of clouds and rain using a z -coordinate nonhydrostatic model. *Mon. Wea. Rev.*, **134**, 3625–3643.
- Sundqvist, H., 1976: On vertical interpolation and truncation in connection with use of sigma system models. *Atmosphere*, **14**, 37–52.
- Tapp, M. C., and P. W. White, 1976: A non-hydrostatic mesoscale model. *Quart. J. Roy. Meteor. Soc.*, **102**, 277–296.
- Thuburn, J., N. Wood, and A. Staniforth, 2002: Normal modes of deep atmospheres. II: f - F -plane geometry. *Quart. J. Roy. Meteor. Soc.*, **128**, 1793–1806.
- Yamazaki, H., and T. Satomura, 2010: Nonhydrostatic atmospheric model using a combined Cartesian grid. *Mon. Wea. Rev.*, **138**, 3932–3945.